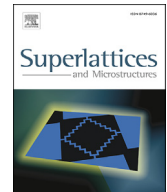




Contents lists available at ScienceDirect

Superlattices and Microstructures

journal homepage: www.elsevier.com/locate/superlattices

A breakdown enhanced AlGaIn/GaN MISFET with source-connected P-buried layer

Xin Luo ^a, Ying Wang ^{b,*}, Fei Cao ^b, Cheng-Hao Yu ^b, Xin-Xing Fei ^a^a College of Information and Communication Engineering, Harbin Engineering University, 150001 Harbin, China^b Key Laboratory of RF Circuits and Systems, Ministry of Education, Hangzhou Dianzi University, 310018 Hangzhou, China

ARTICLE INFO

Article history:

Received 10 July 2017

Received in revised form 4 October 2017

Accepted 4 October 2017

Available online xxx

Keywords:

Source connected P-Buried layer (SC-PBL)

TCAD

MISFET

Figure of merit

Breakdown enhanced

GaN

ABSTRACT

This paper presents a breakdown-enhanced AlGaIn/GaN MISFET with a source-connected P-buried layer combined with field plates (SC-PBL FPs MISFET). A TCAD tool was used to analyze the breakdown characteristics of the proposed structure, and results show that in comparison to the conventional gate field plate MISFET (GFP-C MISFET), the proposed structure provides a significant increase of breakdown voltage (V_{BK}) due to redistribution of electric field in the gate-drain region induced by the SC-PBL and the FPs. The optimized SC-PBL FPs MISFET with a gate-drain spacing of 6 μm achieved a high Baliga's figure of merit of 2.6 GW cm^{-2} with a corresponding breakdown voltage (V_{BK}) of 1311.62 V and specific on resistance ($R_{ON,sp}$) of 0.66 $\text{m}\Omega \text{ cm}^2$, which demonstrates a good trade-off between $R_{ON,sp}$ and V_{BK} compared to the GFP-C MISFET with V_{BK} of 524.27 V and $R_{ON,sp}$ of 0.61 $\text{m}\Omega \text{ cm}^2$.

© 2017 Elsevier Ltd. All rights reserved.

1. Introduction

In power switching applications, AlGaIn/GaN based field effect transistors have been widely studied for their excellent features [1–5], such as high switching speed, high critical electric field, and high density of two-dimensional electron gas (2DEG) originating from the polarization effect [6]. However, the residual donors in the GaN buffer layer, such as oxygen and silicon, which are consequences of the actual growth process, are always present and lead to obvious leakage current and premature breakdown [7]. Several approaches were proposed to reduce buffer leakage current and to improve the breakdown voltage (V_{BK}). The Fe-doped buffer [8–11] and C-doped buffer [12–15] were proposed to compensate the background donors, while an AlGaIn back-barrier layer was proposed to confine the two-dimensional electron gas (2DEG) [16–18]. Regardless of the methods used, there is always a trade-off with the specific on resistance ($R_{ON,sp}$) because of the decrease of 2DEG concentration.

Hitherto, the highest Baliga's figure of merit for lateral GaN devices of 2.3 GW cm^{-2} was achieved using a high-density C-doped compensated buffer layer [19]. However, high concentration C dopants used to improve the breakdown voltage can also cause a significant degradation of $R_{ON,sp}$ due to their trapping effects on 2DEG in the whole channel [20]. In this work, a novel lateral metal-insulator-semiconductor field effect transistor (MISFET) based on a source-connected P-buried layer (SC-PBL) partially inserted in buffer layer combined with field plates (FPs) on the electrodes is proposed, analyzed through 2D-simulation using TCAD tools. The SC-PBL combined with FPs can modulate the potential distribution in the gate-drain region

* Corresponding author.

E-mail address: wangying7711@yahoo.com (Y. Wang).

to enhance V_{BK} while only partially affecting the 2DEG distribution in the channel, thus achieving a satisfactory trade-off between $R_{ON,sp}$ and V_{BK} . A partially P-doped buffer layer had been successfully implemented in many reported works [21–26]. Additionally, PBL in the buffer layer had been deeply studied in vertical devices by the way of simulation [27–29], but not in lateral device, so in this work its impact on the performance of lateral device is systematically studied.

This paper is organized as follows. In Section 2, the structure of the proposed MISFET and simulation set-up are introduced and a brief summary of process steps for the proposed device is given. The breakdown characteristics for three different MISFETs are presented to explain the breakdown improvement achieved by SC-PBL and drain field plate (DFP). Furthermore, basic DC characteristics are also demonstrated. In Section 3, the dependences of V_{BK} , Baliga's figure of merit (BFOM, defined as $V_{BK}^2/R_{ON,sp}$) and $R_{ON,sp}$ on the PBL's location and doping concentration are analyzed and the electric field modulation is used to explain the impact of PBL location on V_{BK} . In addition, the optimization of DFP is presented based on the BFOM criterion. Lastly, in Section 4, the paper is concluded.

2. Structure, simulation set up and device characteristics

2.1. Device structure

The cross-sections of the proposed AlGaIn/GaN MISFET with a source-connected P-buried layer combined with field plates, i.e. SC-PBL FPs MISFET, and a conventional MISFET with gate field, i.e. GFP-C MISFET, are illustrated in Fig. 1. Additionally, a MISFET with source connected P-buried layer, i.e. a SC-PBL GFP MISFET, which will be used to understand the different impacts of SC-PBL and DFP on breakdown performance, is also presented in the figure.

These structures have an unintentionally doped $Al_{0.25}Ga_{0.75}N$ barrier layer, an unintentionally doped GaN channel layer, a GaN middle buffer layer and a GaN bottom buffer layer. The barrier and channel layers under the gate are fully etched to realize normally off operation [29–31], and Si_3N_4 is used as gate dielectric and passivation layers [31] with the thicknesses of 20 nm and 100 nm, respectively. The proposed device additionally has a source-connected P-doped buried region inserted in the buffer layer and a drain field plate.

The buffer layer consists of a bottom buffer layer and a middle buffer layer [32]. The donor concentration of both layers is set to $1 \times 10^{16} \text{ cm}^{-3}$ to emulate background carriers induced by actual growth process. The acceptor type traps are introduced into buffer layers to deplete the background carriers. The bottom buffer layer with higher acceptor trap density $N_{tb} = 4 \times 10^{18} \text{ cm}^{-3}$ can suppress the vertical substrate leakage current effectively, whereas the middle buffer layer with a lower acceptor trap concentration $N_{tm} = 2 \times 10^{16} \text{ cm}^{-3}$ can reduce the lateral leakage current in the buffer layer. An acceptor trap with energy level of 0.86–0.93 eV from GaN valence band had been frequently measured in C-compensated GaN [33–37]. Therefore, in this work, an acceptor trap level at 0.9 eV from GaN valence band [32,35–37] with a cross-section σ_n of $1.3 \times 10^{-14} \text{ cm}^{-2}$ [32] is used.

The details of key structural parameters of the GFP-C MISFET and the proposed SC-PBL FPs MISFET are summarized in Table 1. As shown in Fig. 1(b), L_d is the length of section for which PBL exceeds the right gate edge, and a negative L_d means that the right side of the PBL is on the left of the gate. Furthermore, T_s is the spacing between the PBL and the channel layer, N_{PBL} is the

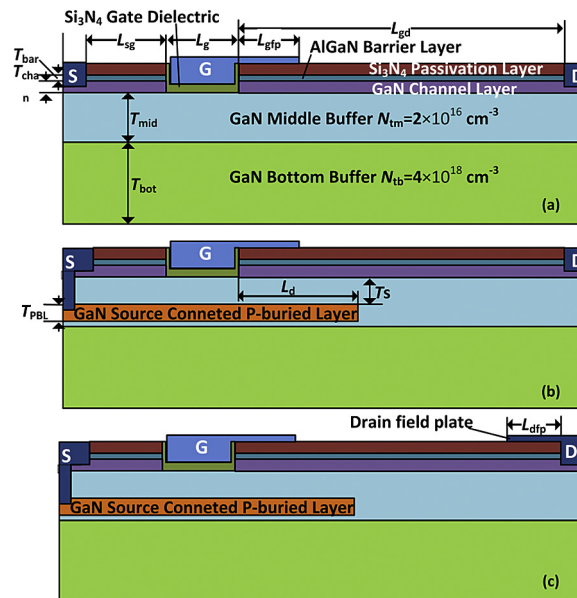


Fig. 1. Cross-section of: (a) GFP-C MISFET, (b) SC-PBL GFP MISFET for comparison and (c) proposed SC-PBL FPs MISFET.

Table 1
Key structural parameters.

Parameters	Unit	Values
Gate-source spacing (L_{gs})	μm	0.5
Gate Length (L_g)	μm	0.5
Gate-drain spacing (L_{gd})	μm	6
Gate field plate length (L_{gfp})	μm	0.5
Bottom buffer layer thickness (T_{bot})	μm	1.6
Middle buffer layer thickness (T_{mid})	μm	0.4
Channel layer thickness (T_{chan})	nm	50
Barrier layer thickness (T_{bar})	nm	25
Length of PBL exceeding right gate edge (L_d)	μm	$-0.4-2^*$
PBL and channel layer spacing (T_s)	μm	$0.05+0.3^*$
Thickness of PBL (T_{PBL})	μm	0.1^*
PBL doping concentration (N_{PBL})	cm^{-3}	$1 \times 10^{17} \pm 5 \times 10^{17*}$
Drain field plate length (L_{dfp})	μm	$0.4-2^*$

Note: Parameters marked with * are only for proposed structure.

doping concentration of PBL and is set in the range $1 \times 10^{17} \text{cm}^{-3} \sim 5 \times 10^{17} \text{cm}^{-3}$ [26]. $L_{gfp} = 0.5 \mu\text{m}$ is optimal value for GFP-C MISFET to achieve highest V_{BK} and the workfunction for the gate metal used in this work is 5.15 eV [38].

In order to explain how the proposed device can be implemented, Fig. 2 presents a brief schematic of the fabrication process steps.

The corresponding description of these process steps is summarized as follows.

- The base structure includes a Mg-doped GaN layer on top of a GaN middle buffer layer and a GaN bottom buffer layer. An epitaxial p-type layer can be realized using metalorganic chemical vapor deposition (MOCVD) using Mg as a p-type impurity [23–25].
- The right part of p-type layer is etched through an inductively coupled plasma (ICP) process [23–25] until the middle buffer layer is exposed.
- The epitaxial middle buffer layer is regrown on the remaining p-type layer and the middle buffer layer. The epitaxial undoped channel layer is then grown on the middle buffer layer, followed by epitaxial undoped barrier layer, and passivation layer.

2-D physics-based numerical simulations for these structures were performed using the TCAD software Sentaurus from Synopsys Inc. A number of models [39–41] were used, such as for instance recombination models, e.g. SRH, Auger and mobility models, e.g. DopingDep and Highfieldsaturation. Furthermore, a polarization model including the GateDependent strain was also included. The effectiveness of these models was validated by simulation of the conventional structure with all parameters from experimental results [31], in which the gate-drain spacing took the value of $15 \mu\text{m}$. As shown in Fig. 3, a R_{ON} value of $12.8 \Omega \text{mm}$ from the I_D - V_{DS} characteristic in Sentaurus simulation was fit well with the experimental results with R_{ON} value of $13.2 \Omega \text{mm}$.

When the breakdown performance was simulated, an Avalanche model with a dependent electric field was additionally included in recombination models. The impact ionization rate is defined in Equation (1) [41]:

$$G = \alpha_n n v_n + \alpha_p p v_p$$

$$\text{Where } \alpha_{n,p} = \gamma_{n,p} a_{n,p} \exp\left(-b_{n,p} \gamma_{n,p} / E\right) \quad (1)$$

n, p are the electron and hole concentration, respectively, while v_n, v_p refer to the respective saturation velocities. The value of the impact-ionization coefficients α_n and α_p are related to the electric field. γ_n and γ_p express the temperature dependence of the phonon gas against which carriers are accelerated. The coefficients a_n, a_p, b_n and b_p are the fitting parameters. a_n and b_n were set to $2.9 \times 10^8 \text{cm}^{-1}$ and $3.4 \times 10^7 \text{V/cm}$, respectively [42], while a_p and b_p were set to their default value as used in the Sentaurus material database [39].

2.2. Principle of breakdown enhancement

The breakdown characteristics of the GFP-C MISFET, SC-PBL GFP MISFET and the SC-PBL FPs MISFET with $L_d = 0.5 \mu\text{m}, T_s = 0.15 \mu\text{m}, N_{PBL} = 1 \times 10^{17} \text{cm}^{-3}$ and $L_{dfp} = 1.7 \mu\text{m}$ are presented in Fig. 4. The V_{BK} s were extracted for a drain leakage current of $0.01 \mu\text{A/mm}$ when $V_{GS} = 0 \text{V}$. Compared to the V_{BK} of 524.7 V in GFP-C MISFET, an improved V_{BK} of 774.9 V was achieved in the SC-PBL GFP MISFET and a further enhanced V_{BK} of 1043 V was obtained in SC-PBL FPs MISFET. A reduction in leakage current is shown in Fig. 4(a), wherein the leakage current in the proposed MISFET is lower than that of the GFP-C MISFET when $V_{DS} = 300 \text{V}$.

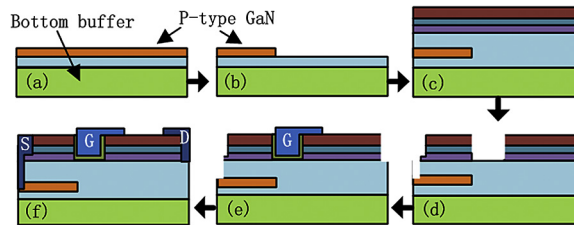


Fig. 2. Schematic of fabrication process steps for proposed structure.

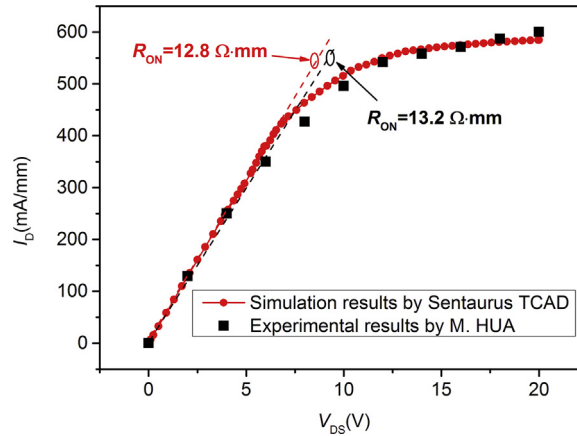


Fig. 3. The I_D - V_{DS} characteristics from simulation and experiment validate the effectiveness of models in simulation.

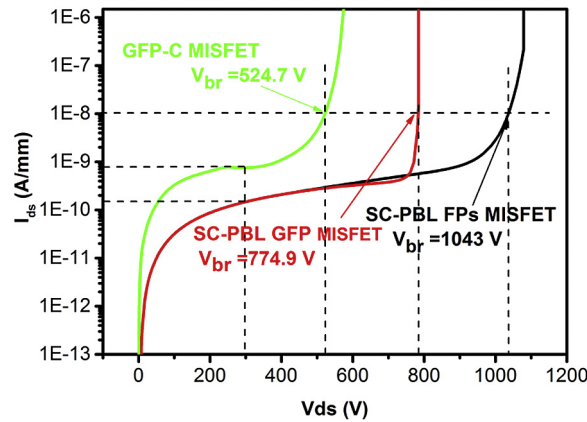


Fig. 4. The breakdown characteristics of GFP-C MISFET, SC-PBL GFP MISFET and SC-PBL FPs MISFET.

In order to explain the improvement of breakdown characteristics, the equipotential line profiles of the three devices when $V_{DS} = V_{BK}$ are shown in Fig. 5. In the GFP-C MISFET, the equipotential lines in the channel stop at the position A, which indicates that the 2DEG is hardly depleted and nearly no space charge region is created from A to drain when breakdown occurs. When the SC-PBL is introduced in the SC-PBL GFP MISFET, Fig. 5 (b), the equipotential lines spread all over the gate-drain region. The PBL combined with the low-doped traps buffer and channel layers can be considered as a reverse-biased p-i-n diode, which can help the expansion of the space charge region. However, the equipotential line near the drain is still loose, implying that the gate-drain region is not adequately utilized for voltage sharing. As shown in Fig. 5 (c), the equipotential lines in SC-PBL FPs MISFET become more compact and are nearly uniformly distributed, which suggests that the introduction of DFP can help make the gate-drain region more efficiently and further enhance V_{BK} .

A cutline of the horizontal electric field distribution for each device was made in the 2DEG channel at 1 nm away from the heterojunction interface, as shown in Fig. 5 (d). In the GFP-C MISFET, the electric field peak appears at position A and the field

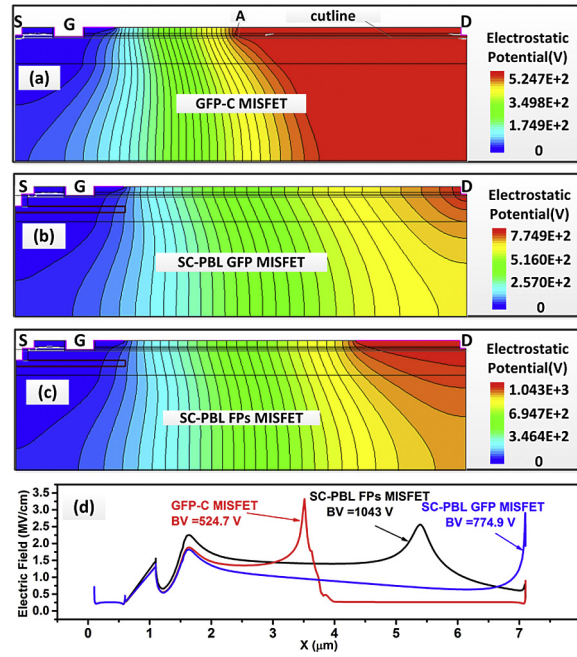


Fig. 5. The equipotential line profile of: (a) GFP-C MISFET, (b) SC-PBL GFP MISFET, (c) SC-PBL FPs MISFET when breakdown occurs, and (d) the corresponding horizontal electric field distribution in 2DEG area.

decreases sharply to a very low value on the left side of A. In the SC-PBL GFP MISFET, the electric field peak at position A disappears, and a new peak appears on the drain edge because of the space charge region extension. Moreover, the electric field profile in the gate-drain region becomes flat, and as a consequence, V_{BK} is improved. In the SC-PBL FPs MISFET, the electric field near the drain decreases and a new field peak emerges below the DFP due to electric field modulation. The electric field profile in the gate-drain region is further strengthened and consequently, V_{BK} is raised even further.

Fig. 6(a) shows a comparison of the I_D - V_G characteristic of an optimized SC-PBL FPs MISFET with that of the conventional MISFET; here, V_{TH} is shifted from 2.30 to 4.4 V. This shift is due to the higher band energy under the gate, which is induced by the inserted P-buried layer, demonstrating that the SC-PBL FPs MISFET allows for safer in power switching applications. Meanwhile, the higher band energy in an EC-PIN MISFET can also suppress the electron leakage current from the channel to the buffer layer under the P-buried layer, leading to a smaller total leakage current when compared to conventional MISFETs, which is shown in Fig. 4(a). Fig. 6(b) shows that because the PBL only affects part of the 2DEG, R_{ON} increases from 8.52 Ω mm to only 8.84 Ω mm. Accordingly, the calculated specific on-resistance ($R_{ON,sp}$), which is defined as R_{ON} multiplied by the active area [19], only increases from 0.61 m Ω cm² to 0.64 m Ω cm².

3. Discussion and optimization

In this section, simulations with various parameters are presented to analyze the influence of PBL and DFP on breakdown characteristic. There are three key parameters for PBL, i.e. N_{PBL} , L_d and T_s , while for DFP the key parameter is the length of DFP, i.e. L_{dfp} . In order to investigate the impact of PBL parameters on the breakdown characteristic of proposed device and to optimize their values, L_{dfp} was initially set to 1.7 μ m.

3.1. Dependence of breakdown characteristic on location of PBL

Initially, the impact of PBL location on breakdown performance was analyzed. N_{PBL} was fixed to 3×10^{17} cm⁻³ and T_s varied in the range of 0.05–0.3 μ m with a step size of 0.05 μ m, the behavior of $R_{ON,sp}$, V_{BK} , and BFOM on L_d ranged from -0.4 μ m to 2 μ m with a step of 0.3 μ m, was investigated. The results are shown in Figs. 7(a) and 8(a, b), respectively.

In Fig. 7(a), $R_{ON,sp}$ demonstrates a linear increase when $L_d > 0$ μ m because of the depletion of the 2DEG induced by the diffusion of holes from PBL. When these linear regions are fitted with linear curves, the slope of these linear curves increases with an decreasing T_s , meaning that with as increasing T_s s, more 2DEG per unit length of PBL will be depleted. 2DEG depletion can be observed intuitively from the horizontal distribution of the 2DEG density shown in Fig. 7(b). Because there is no PBL existing from 4 μ m to 7 μ m, the electron density distribution in the x-axes from 0 μ m to 4 μ m is shown to illustrate the change of 2DEG density more clearly. When $T_s = 0.1$ μ m, as $L_d = -0.1$ μ m, the PBL cannot deplete the 2DEG on left of the gate in the channel, but there is still a decrease in electron density due to the accumulated electrical field of the GFP, as reported in

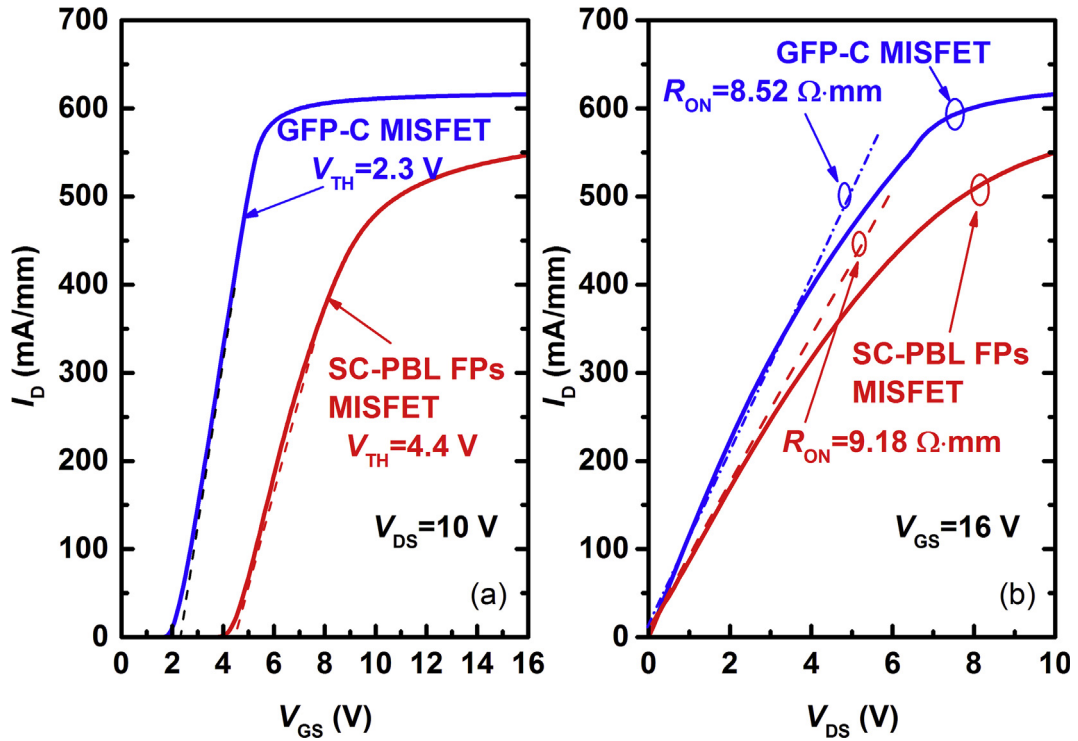


Fig. 6. (a) I_D - V_{GS} characteristics at $V_{DS} = 10$ V, and (b) I_D - V_{DS} characteristics at $V_{GS} = 16$ V for GFP-C MISFET and SC-PBL FPs MISFET.

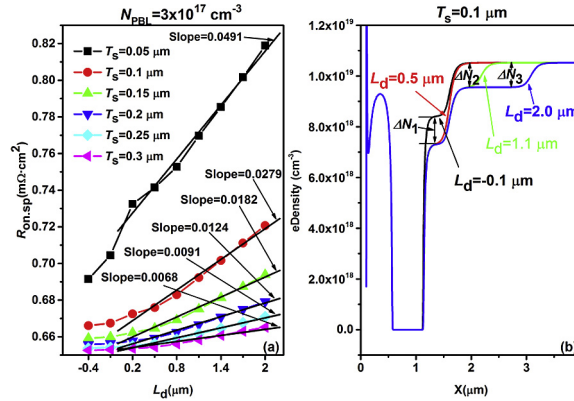


Fig. 7. (a) Calculated $R_{ON,sp}$ for different T_s (0.05–0.3 μm), constant N_{PBL} ($3 \times 10^{17} \text{ cm}^{-3}$) vary on L_d in range of $-0.4 \mu\text{m}$ – $2.0 \mu\text{m}$ and (b) the 2DEG density distribution in X axes from 0 μm to 4 μm for $T_s = 0.1 \mu\text{m}$, $N_{PBL} = 3 \times 10^{17} \text{ cm}^{-3}$ and $L_d = -0.1 \mu\text{m}$, $0.5 \mu\text{m}$, $1.1 \mu\text{m}$ and $2.0 \mu\text{m}$.

Ref. [16]. As L_d increases to the length of the GFP (0.5 μm), more electrons below the GFP are depleted, and when the PBL gets longer, the 2DEG in longer distance in the channel will be depleted at a longer distance. The concentration decrements ΔN_1 , ΔN_2 and ΔN_3 shown in Fig. 7(b) are $1.08 \times 10^{18} \text{ cm}^{-3}$, $1.05 \times 10^{18} \text{ cm}^{-3}$ and $1.06 \times 10^{18} \text{ cm}^{-3}$, respectively. The small difference between these three values could explain the linear increase of $R_{ON,sp}$ with an increasing L_d .

Fig. 8(a) shows that when L_d increases from $-0.4 \mu\text{m}$ to $-0.1 \mu\text{m}$, V_{BK} will be greatly increased, and a smaller T_s can lead to a higher V_{BK} . V_{BK} curves for $T_s = 0.05 \mu\text{m}$ – $0.25 \mu\text{m}$ demonstrate a saturation state when $L_d = 0.2 \mu\text{m}$ to L_d with specific values such as $1.1 \mu\text{m}$, $0.8 \mu\text{m}$ and $0.5 \mu\text{m}$ as L_d exceeds these values, V_{BK} decreases. However, for $T_s = 0.3 \mu\text{m}$ a peak occurs instead of a saturation region. The specific value for $T_s = 0.05$ – $0.15 \mu\text{m}$ is $1.1 \mu\text{m}$, but for $T_s = 0.2 \mu\text{m}$ and $T_s = 0.25 \mu\text{m}$ is $0.8 \mu\text{m}$ and $0.5 \mu\text{m}$, respectively. A mechanism of electric field distribution modulation by PBL is proposed to interpret these trends.

A high electric field region exists around the PBL/middle buffer layer interface and this region affects high electrical field region induced by the GFP, consequently modulating the electric field profile and V_{BK} . This modulation depends on T_s . A smaller T_s can deplete the 2DEG more and cause an obvious concentration gradient, which leads to further electric field

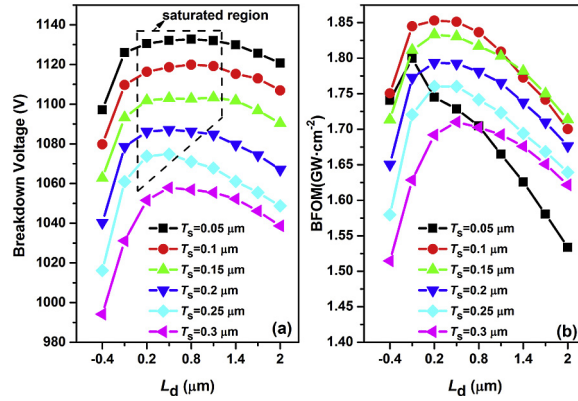


Fig. 8. The dependences of (a) V_{BK} and (b) BFOM on L_d that varies from -0.4 μm to 2 μm with the step size of 0.3 μm for T_s in the range 0.05 – 0.3 μm , $N_{PBL} = 3 \times 10^{17} \text{ cm}^{-3}$.

modulation and higher V_{BK} improvement. This modulation is also dependent on L_d , a phenomenon which can be explained using the cross-section of the electric field's profile which is shown in Fig. 9 for devices with $T_s = 0.1$ μm , $N_{PBL} = 3 \times 10^{17} \text{ cm}^{-3}$ and different L_d values. When $L_d = -0.1$ μm , the high electric field near the interface has almost no influence over the high electric field region below the GFP. However, when L_d is equal to 0.5 μm or 1.1 μm , in actuality, also for $L_d = 0.2$ μm which not shown in Fig. 9, the two high field regions overlap, thus both the electric field profile and V_{BK} are improved. When $L_d = 2.0$ μm , the PBL cannot modulate the electric field profile effectively, so V_{BK} 's improvement is weaker.

Therefore, for V_{BK} curves with T_s in the range 0.05 – 0.25 μm , due to the fact that a strong electric field modulation below the GFP is sustained, V_{BK} s exhibits a saturated state when L_d increases from 0.2 μm to the aforementioned values. As L_d continues to increase, the electric field modulation obviously declines, causing V_{BK} to decrease. However, because an increase of T_s can lead to a reduction of the electric field's modulation, and also cause a faster decrease of V_{BK} , the length of the saturated region will be shortened. Similarly for curve with $T_s = 0.3$ μm , because the electric field modulation is further weakened, the V_{BK} curve only achieves its maximum at $L_d = 0.5$ μm , and it also demonstrates a slower decrease compared to the curves with higher T_s values because when PBL is far away from the channel, the increase of L_d does not lead to an obvious reduction of modulation.

The BFOM curves are shown in Fig. 8(b). The BFOM curves for $T_s = 0.1$ – 0.3 μm achieve to their maximal values as L_d reaches to 0.5 μm , then decrease when $L_d > 0.5$ μm because of the following fact: as L_d increases beyond 0.5 μm , $R_{ON,sp}$ for each T_s continues to increase as shown in Fig. 7(a), but the corresponding V_{BK} s stay saturated or even decrease as shown in Fig. 8(a). However, after achieving the maximum value at $L_d = -0.1$ μm , the $T_s = 0.05$ μm curve demonstrates a steep decrease as L_d continues to increase due to the sharp increase of $R_{ON,sp}$. Furthermore, if we compare the curve with $T_s = 0.1$ μm to that of

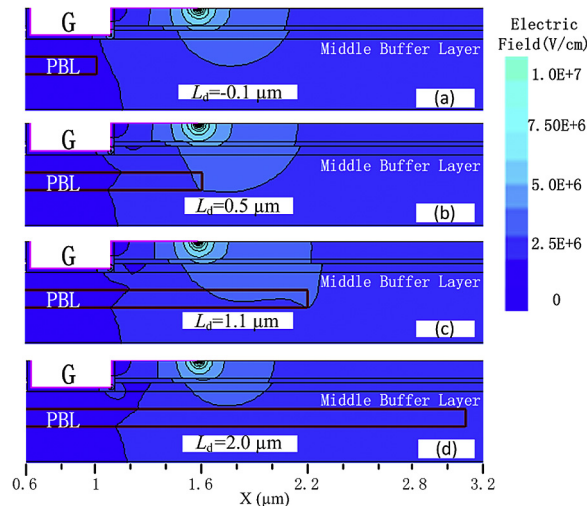


Fig. 9. Electric field profiles around PBL when breakdown occurs for proposed device with $T_s = 0.1$ μm , $N_{PBL} = 3 \times 10^{17} \text{ cm}^{-3}$ and different L_d : (a) $L_d = -0.1$ μm , (b) $L_d = 0.5$ μm , (c) $L_d = 1.1$ μm , and (d) $L_d = 2.0$ μm .

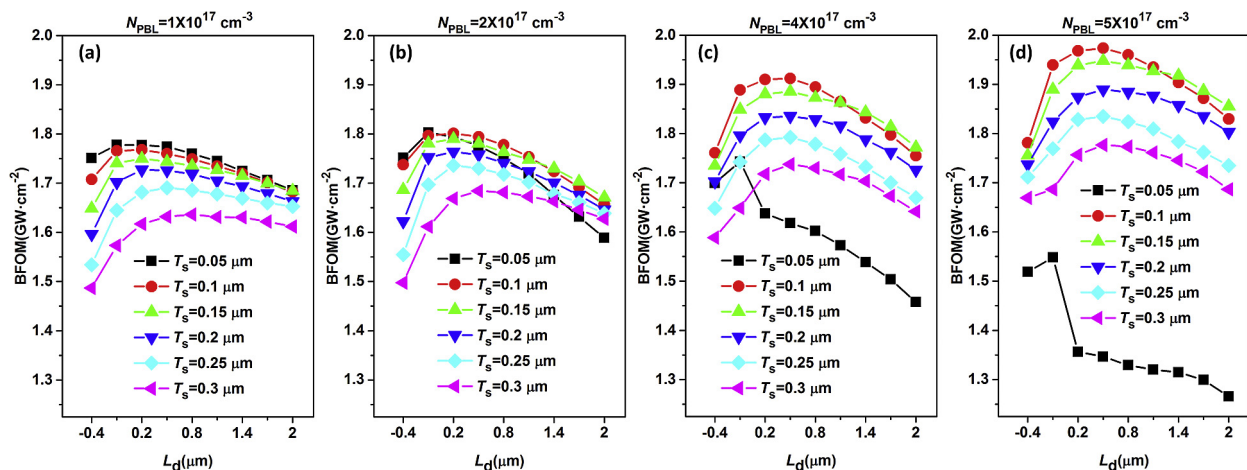


Fig. 10. The dependences of BFOM on L_d that varies from $-0.4 \mu\text{m}$ to $2 \mu\text{m}$ for SC-PBL FPs MISFETs with different T_s (0.05 – $0.3 \mu\text{m}$) and various N_{PBL} : (a) $N_{\text{PBL}} = 1 \times 10^{17} \text{ cm}^{-3}$, (b) $N_{\text{PBL}} = 2 \times 10^{17} \text{ cm}^{-3}$, (c) $N_{\text{PBL}} = 4 \times 10^{17} \text{ cm}^{-3}$, and (d) $N_{\text{PBL}} = 5 \times 10^{17} \text{ cm}^{-3}$.

$T_s = 0.15 \mu\text{m}$, the BFOM in the former is higher when L_d is in the range of $-0.4 \mu\text{m}$ – $1.1 \mu\text{m}$, but lower when $L_d \geq 1.1 \mu\text{m}$, which is attributed to the steeper increase of $R_{\text{ON,sp}}$.

To investigate the influence of N_{PBL} on BFOM, more simulations were performed for devices whose N_{PBL} varied from $1 \times 10^{17} \text{ cm}^{-3}$ to $5 \times 10^{17} \text{ cm}^{-3}$ except $3 \times 10^{17} \text{ cm}^{-3}$ because devices with $N_{\text{PBL}} = 3 \times 10^{17} \text{ cm}^{-3}$ have been investigated in subsection 3.1. The BFOMs of these devices are demonstrated in Fig. 10. For devices with $T_s = 0.05 \mu\text{m}$ (black squares curves), BFOMs degrade quickly when L_d increases from $-0.1 \mu\text{m}$ to $0.2 \mu\text{m}$, and this effect is particularly pronounced for higher N_{PBL} values. To explore the reason of this phenomenon, the dependencies of $R_{\text{ON,sp}}$ and V_{BK} on different L_d for different N_{PBL} when $T_s = 0.05 \mu\text{m}$ are shown in Fig. 11. In this case, $R_{\text{ON,sp}}$ increases sharply when L_d increases from $-0.1 \mu\text{m}$ to $0.2 \mu\text{m}$, especially for higher N_{PBL} values; however, the magnitudes of the corresponding V_{BK} don't increase so obviously, resulting in a sharp decrease of BFOMs ($V_{\text{BK}}^2/R_{\text{ON,sp}}$). Fig. 11 also shows the dependence of $R_{\text{ON,sp}}$ and V_{BK} on N_{PBL} . Higher N_{PBL} values will yield higher $R_{\text{ON,sp}}$ and V_{BK} values due to the depletion of 2DEG and enhanced electric field modulation.

Returning to Fig. 10, we see that the curves with N_{PBL} values of $2 \times 10^{17} \text{ cm}^{-3}$, $4 \times 10^{17} \text{ cm}^{-3}$ and $5 \times 10^{17} \text{ cm}^{-3}$ are similar to the curves with $N_{\text{PBL}} = 3 \times 10^{17} \text{ cm}^{-3}$ in Fig. 8(b), for $T_s = 0.1 \mu\text{m}$, BFOMs are smaller than those for $T_s = 0.15 \mu\text{m}$ when $L_d \geq 1.1 \mu\text{m}$. Nevertheless, for $N_{\text{PBL}} = 1 \times 10^{17} \text{ cm}^{-3}$, a smaller T_s always yields a higher BFOM because a PBL with low N_{PBL} rarely depletes the 2DEG in the channel, leading to no obvious degradation of $R_{\text{ON,sp}}$. In Fig. 10, the highest BFOM of 1.97 GW cm^{-2} is achieved for $N_{\text{PBL}} = 5 \times 10^{17} \text{ cm}^{-3}$, $T_s = 0.1 \mu\text{m}$ and $L_d = 0.5 \mu\text{m}$, which are the optimized parameters for the PBL.

3.2. Optimization of L_{dfp}

The optimization of L_{dfp} was performed using a device with optimized PBL parameters. The values of V_{BK} s and corresponding BFOMs are shown in Fig. 12(a). According to the results, when the L_{dfp} is equal to $0.8 \mu\text{m}$, V_{BK} and BFOM have their

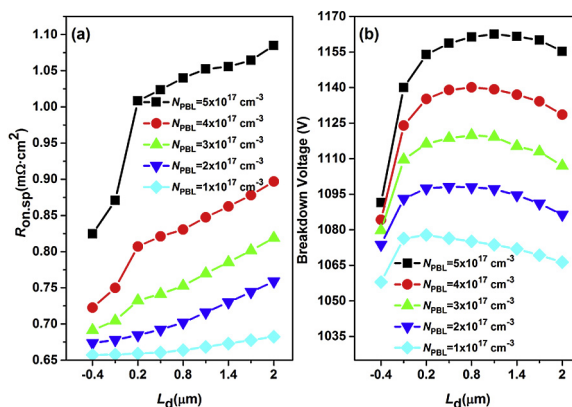


Fig. 11. (a) Calculated $R_{\text{ON,sp}}$ and (b) BFOM vary on L_d ranging from $-0.4 \mu\text{m}$ to $2.0 \mu\text{m}$ with a step size of $0.3 \mu\text{m}$ and N_{PBL} ranging from $1 \times 10^{17} \text{ cm}^{-3}$ to $5 \times 10^{17} \text{ cm}^{-3}$ with a step size of $1 \times 10^{17} \text{ cm}^{-3}$ while $T_s = 0.05 \mu\text{m}$.

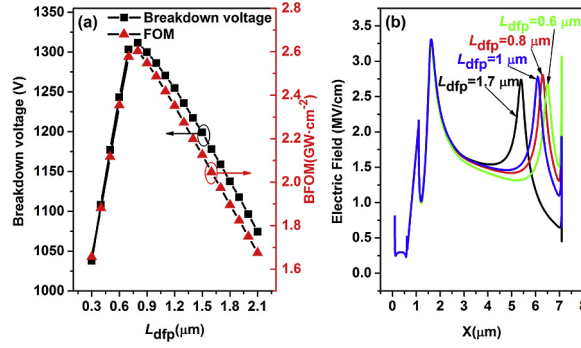


Fig. 12. (a) The dependence of BFOM and V_{BK} on L_{dfp} for proposed MISFETs with $N_{PBL} = 5 \times 10^{17} \text{ cm}^{-3}$, $T_s = 0.1 \text{ μm}$ and $L_d = 0.5 \text{ μm}$, and (b) the horizontal distribution of electric field cut in 2DEG area for devices with $L_{dfp} = 0.6 \text{ μm}$, 0.8 μm , 1.0 μm and 1.7 μm .

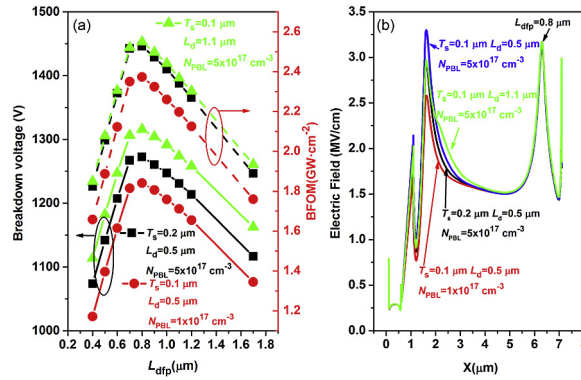


Fig. 13. (a) The dependence of BFOM and V_{BK} on L_{dfp} for SC-PBL FPs MISFETs with different PBL parameters, and (b) the horizontal distribution of electric field in 2DEG area for these MISFETs when $L_{dfp} = 0.8 \text{ μm}$.

maxima of 1311.62 V and 2.6 GW cm^{-2} , respectively. In Fig. 12(b), the horizontal electric field profiles in the 2DEG area are shown for $L_{dfp} = 0.6 \text{ μm}$, 0.8 μm , 1.0 μm and 1.7 μm , respectively. It is evident that the electric field profile above PBL is not affected with the variation of the drain field plate's length, which indicates that the PBL and DFP parameters may be optimized separately.

In order to verify this conclusion, the dependence of V_{BK} and BFOM on L_{dfp} for different PBL parameters were studied, and the results are shown in Fig. 13(a), wherein the green triangles donate devices with $N_{PBL} = 5 \times 10^{17} \text{ cm}^{-3}$, $T_s = 0.1 \text{ μm}$, $L_d = 1.1 \text{ μm}$, black squares represent devices with $N_{PBL} = 5 \times 10^{17} \text{ cm}^{-3}$, $T_s = 0.2 \text{ μm}$, $L_d = 0.5 \text{ μm}$ and red circles are devices with $N_{PBL} = 1 \times 10^{17} \text{ cm}^{-3}$, $T_s = 0.1 \text{ μm}$, $L_d = 0.5 \text{ μm}$. In this figure, one of PBL parameters is changed while other two parameters maintain their optimized values. However, for all devices, both V_{BK} curves and BFOM curves obtain the maximum value when $L_{dfp} = 0.8 \text{ μm}$. In Fig. 13(b), the horizontal electric field distribution in the 2DEG area is extracted from these three devices when $L_{dfp} = 0.8 \text{ μm}$ and $V_{DS} = V_{BK}$, and the field distribution in the optimized device is also presented for reference. Although the PBL have different parameters, no change occurs in the electric field distribution below the DFP, which further validates that PBL and DFP parameters can be optimized separately due to their independent influence on the electric field's profile in the gate-drain region.

4. Conclusions

In this paper, a normally-off AlGaIn/GaN MISFET with a source-connected P-buried layer combined with field plates (SC-PBL FPs MISFET) is presented and simulated. The breakdown characteristics of a GFP-C MISFET, a SC-PBL GFP MISFET and a SC-PBL FPs MISFET were simulated in order to interpret the improvement principles of the PBL and the DFP. A mechanism of electric field modulation by the PBL is used to explain the impact of the PBL's location on V_{BK} . The closer the PBL is to 2DEG, the higher V_{BK} improvement was achieved because of the increased depletion of the 2DEG and consequent improvement of the electric field. As the length of the PBL increases, V_{BK} increases until it reaches saturation and then decreases due to the change of electric field modulation; however, the $R_{ON,sp}$ increases constantly. The parameters of the PBL and DFP were optimized to obtain the highest BFOM for the proposed SC-PBL FPs MISFET. An optimized device with $L_{gd} = 6 \text{ μm}$ exhibits a

BFOM of 2.6 GW cm^{-2} , V_{BK} of 1311.62 V and a $R_{\text{ON,sp}}$ of $0.66 \text{ m}\Omega \text{ cm}^2$, which represents a 150% improvement of V_{BK} and only 8.2% degradation of $R_{\text{ON,sp}}$ in comparison to the GFP-C MISFET. A good trade-off between $R_{\text{ON,sp}}$ and V_{BK} suggests that the proposed SC-PBL FPs MISFET represents a good alternative structure for switching applications.

Acknowledgements

This work was supported by the National Natural Science Foundation of China (No. 51371063) and the Excellent Youth Foundation of Zhejiang Province of China (No. LR17F040001).

References

- [1] M. Ishida, T. Ueda, T. Tanaka, D. Ueda, GaN on Si technologies for power switching devices, *IEEE Trans. Electron Dev.* 60 (2013) 3053–3059, <https://doi.org/10.1109/TED.2013.2268577>.
- [2] K.J. Chen, O. Haberen, A. Lidow, C. Lin Tsai, T. Ueda, Y. Uemoto, Y. Wu, GaN-on-Si power technology: devices and applications, *IEEE Trans. Electron Dev.* 64 (2017) 779–795, <https://doi.org/10.1109/TED.2017.2657579>.
- [3] B.J. Baliga, Gallium nitride devices for power electronic applications, *Semicond. Sci. Technol.* 28 (2013), 074011, <https://doi.org/10.1088/0268-1242/28/7/074011>.
- [4] A. Nakajima, K. Takao, H. Ohashi, GaN power transistor modeling for high-speed converter circuit design, *IEEE Trans. Electron Dev.* 60 (2013) 646–652, <https://doi.org/10.1109/TED.2012.2226180>.
- [5] W. Saito, Y. Takada, M. Kuraguchi, K. Tsuda, I. Omura, T. Ogura, H. Ohashi, High breakdown voltage AlGaIn/GaN power-HEMT design and high current density switching behavior, *IEEE Trans. Electron Dev.* 50 (2003) 2528–2531, <https://doi.org/10.1109/TED.2003.819248>.
- [6] O. Ambacher, J. Smart, J.R. Shealy, N.G. Weimann, K. Chu, M. Murphy, W.J. Schaff, L.F. Eastman, R. Dimitrov, L. Wittmer, M. Stutzmann, W. Rieger, J. Hilsenbeck, Two-dimensional electron gases induced by spontaneous and piezoelectric polarization charges in N- and Ga-face AlGaIn/GaN heterostructures, *J. Appl. Phys.* 85 (1999) 3222–3233, <https://doi.org/10.1063/1.369664>.
- [7] C. Zhou, Q. Jiang, S. Huang, K.J. Chen, Vertical leakage/breakdown mechanisms in AlGaIn/GaN-on-Si devices, *IEEE Electron Device Lett.* 33 (2012) 1132–1134, <https://doi.org/10.1109/LED.2012.2200874>.
- [8] Y.C. Choi, M. Pophristic, H.-Y. Cha, B. Peres, M.G. Spencer, L.F. Eastman, The effect of an Fe-doped GaN buffer on off-state breakdown characteristics in AlGaIn/GaN HEMTs on Si substrate, *IEEE Trans. Electron Dev.* 53 (2006) 2926–2931, <https://doi.org/10.1109/TED.2006.885679>.
- [9] V. Desmaris, M. Rudzinski, N. Rorsman, P.R. Hageman, P.K. Larsen, H. Zirath, T.C. Rodle, H.F.F. Jos, Comparison of the DC and microwave performance of AlGaIn/GaN HEMTs grown on SiC by MOCVD with Fe-Doped or unintentionally doped GaN buffer layers, *IEEE Trans. Electron Dev.* 53 (2006) 2413–2417, <https://doi.org/10.1109/TED.2006.880825>.
- [10] O. Axelsson, S. Gustafsson, H. Hjelmgren, N. Rorsman, H. Blanck, J. Splettstoesser, J. Thorpe, T. Roedle, M. Thorsell, Application relevant evaluation of trapping effects in AlGaIn/GaN HEMTs with Fe-Doped buffer, *IEEE Trans. Electron Dev.* 63 (2016) 326–332, <https://doi.org/10.1109/TED.2015.2499313>.
- [11] M. Meneghini, I. Rossetto, D. Bisi, A. Stocco, A. Pantellini, C. Lanzieri, A. Nanni, G. Meneghesso, E. Zanoni, Buffer traps in Fe-Doped AlGaIn/GaN HEMTs: investigation of the physical properties based on pulsed and transient measurements, *IEEE Trans. Electron Dev.* 61 (2014) 4070–4077, <https://doi.org/10.1109/TED.2014.2364855>.
- [12] C. Poblenz, P. Waltereit, S. Rajan, S. Heikman, U.K. Mishra, J.S. Speck, Effect of carbon doping on buffer leakage in AlGaIn/GaN high electron mobility transistors, *J. Vac. Sci. Technol. B Microelectron. Nanom. Struct.* 22 (2004) 1145, <https://doi.org/10.1116/1.1752907>.
- [13] S. Kato, Y. Satoh, H. Sasaki, I. Masayuki, S. Yoshida, C-doped GaN buffer layers with high breakdown voltages for high-power operation AlGaIn/GaN HFETs on 4-in Si substrates by MOVPE, *J. Cryst. Growth* 298 (2007) 831–834, <https://doi.org/10.1016/j.jcrysgro.2006.10.192>.
- [14] M.J. Uren, M. Silvestri, M. Casar, G.A.M. Hurkx, J.A. Croon, J. Sonsky, M. Kuball, Intentionally carbon-doped AlGaIn/GaN HEMTs: necessity for vertical leakage paths, *IEEE Electron Device Lett.* 35 (2014) 327–329, <https://doi.org/10.1109/LED.2013.2297626>.
- [15] I. Chatterjee, M.J. Uren, S. Karboyan, A. Pooth, P. Moens, A. Banerjee, M. Kuball, Lateral charge transport in the carbon-doped buffer in AlGaIn/GaN-on-Si HEMTs, *IEEE Trans. Electron Dev.* 64 (2017) 977–983, <https://doi.org/10.1109/TED.2016.2645279>.
- [16] E. Bahat-Treidel, O. Hilt, F. Brunner, V. Sidorov, J. Würfl, G. Tränkle, AlGaIn/GaN/AlGaIn DH-HEMTs breakdown voltage enhancement using multiple grating field plates (MGFPs), *IEEE Trans. Electron Dev.* 57 (2010) 1208–1216, <https://doi.org/10.1109/TED.2010.2045705>.
- [17] D. Visalli, M. Van Hove, J. Derluyn, S. Degroote, M. Leys, K. Cheng, M. Germain, G. Borghs, AlGaIn/GaN/AlGaIn double heterostructures on silicon substrates for high breakdown voltage field-effect transistors with low on-resistance, *Jpn. J. Appl. Phys.* 48 (2009), 04C101, <https://doi.org/10.1143/JJAP.48.04C101>.
- [18] J. Das, J. Everts, J. Van den Keybus, M. Van Hove, D. Visalli, P. Srivastava, D. Marcon, K. Cheng, M. Leys, S. Decoutere, J. Driesen, G. Borghs, A 96% efficient high-frequency DC–DC converter using E-mode GaN DHFETs on Si, *IEEE Electron Device Lett.* 32 (2011) 1370–1372, <https://doi.org/10.1109/LED.2011.2162393>.
- [19] E. Bahat-Treidel, F. Brunner, O. Hilt, E. Cho, J. Würfl, G. Tränkle, AlGaIn/GaN/AlGaIn C back-barrier HFETs with breakdown voltage of over 1 kV and low $R_{\text{ON}} \times A$, *IEEE Trans. Electron Dev.* 57 (2010) 3050–3058, <https://doi.org/10.1109/TED.2010.2069566>.
- [20] P. Moens, P. Vanmeerbeek, A. Banerjee, J. Guo, C. Liu, P. Coppens, A. Salih, M. Tack, M. Caesar, M.J. Uren, M. Kuball, M. Meneghini, G. Meneghesso, E. Zanoni, On the impact of carbon-doping on the dynamic R_{on} and off-state leakage current of 650V GaN power devices, in: 2015 IEEE 27th International Symposium on Power Semiconductor Devices ICs (ISPSD), 2015, pp. 37–40, <https://doi.org/10.1109/ISPSD.2015.7123383>.
- [21] Y. Gao, I. Ben-Yaacov, U.K. Mishra, E.L. Hu, Optimization of AlGaIn/GaN current aperture vertical electron transistor (CAVET) fabricated by photo-electrochemical wet etching, *J. Appl. Phys.* 96 (2004) 6925–6927, <https://doi.org/10.1063/1.1806281>.
- [22] S. Chowdhury, M.H. Wong, B.L. Swenson, U.K. Mishra, CAVET on bulk GaN substrates achieved with MBE-regrown AlGaIn/GaN layers to suppress dispersion, *IEEE Electron Device Lett.* 33 (2012) 41–43, <https://doi.org/10.1109/LED.2011.2173456>.
- [23] D. Ji, M.A. Laurent, A. Agarwal, W. Li, S. Mandal, S. Keller, S. Chowdhury, Normally off trench CAVET with active Mg-doped GaN as current blocking layer, *IEEE Trans. Electron Dev.* 64 (2017) 805–808, <https://doi.org/10.1109/TED.2016.2632150>.
- [24] H. Nie, Q. Diduck, B. Alvarez, A.P. Edwards, B.M. Kayes, M. Zhang, G. Ye, T. Prunty, D. Bour, I.C. Kizilyalli, 1.5-kV and 2.2-m Ω -cm 2 vertical GaN transistors on bulk-GaN substrates, *IEEE Electron Device Lett.* 35 (9) (Sep. 2014) 939–941, <https://doi.org/10.1109/LED.2014.2339197>.
- [25] M. Kanechika, M. Sugimoto, N. Soejima, H. Ueda, O. Ishiguro, M. Kodama, E. Hayashi, K. Itoh, T. Uesugi, T. Kachi, A vertical insulated gate AlGaIn/GaN heterojunction field-effect transistor, *Jpn. J. Appl. Phys.* 46 (21) (May 2007) L503–L505, <https://doi.org/10.1143/JJAP.46.L503>.
- [26] S. Chowdhury, B.L. Swenson, U.K. Mishra, Enhancement and depletion mode AlGaIn/GaN CAVET with Mg-ion-implanted GaN as current blocking layer, *IEEE Electron Device Lett.* 29 (2008) 543–545, <https://doi.org/10.1109/LED.2008.922982>.
- [27] J. Du, D. Liu, Z. Zhao, Z. Bai, L. Li, J. Mo, Q. Yu, Design of high breakdown voltage GaN vertical HFETs with p-GaN buried buffer layers for power switching applications, *Superlattice. Microstruct.* 83 (2015) 251–260, <https://doi.org/10.1016/j.spmi.2015.03.039>.
- [28] J. Du, D. Liu, Z. Bai, Y. Liu, Q. Yu, Design of high breakdown voltage GaN-based vertical HFETs with p-GaN island structure for power applications, *Superlattice. Microstruct.* 85 (2015) 690–696, <https://doi.org/10.1016/j.spmi.2015.06.043>.
- [29] Q. Zhou, Y. Yang, K. Hu, R. Zhu, W. Chen, B. Zhang, Device technologies of GaN-on-Si for power electronics: enhancement-mode hybrid MOS-HFET and lateral diode, *IEEE Trans. Ind. Electron.* (2017), <https://doi.org/10.1109/TIE.2017.2652373>, 1–1.

- [30] W. Choi, O. Seok, H. Ryu, H.-Y. Cha, K.-S. Seo, High-voltage and low-leakage-current Gate recessed normally-Off GaN MIS-HEMTs with dual gate insulator employing PEALD-SiNx/RF-sputtered-HfO₂, *IEEE Electron Device Lett.* 35 (2014) 175–177, <https://doi.org/10.1109/LED.2013.2293579>.
- [31] M. Hua, Z. Zhang, J. Wei, J. Lei, G. Tang, K. Fu, Y. Cai, B. Zhang, K.J. Chen, Integration of LPCVD-SiNx gate dielectric with recessed-gate E-mode GaN MIS-FETs: toward high performance, high stability and long TDD lifetime, in: 2016 IEEE International Electron Devices Meeting (IEDM), 2016, pp. 10.4.1–10.4.4, <https://doi.org/10.1109/IEDM.2016.7838388>.
- [32] A. Chini, G. Meneghesso, M. Meneghini, F. Fantini, G. Verzellesi, A. Patti, F. Lucolano, Experimental and numerical analysis of hole emission process from carbon-related traps in GaN buffer layers, *IEEE Trans. Electron Dev.* 63 (2016) 3473–3478, <https://doi.org/10.1109/TED.2016.2593791>.
- [33] M.J. Uren, M. Căsar, M.A. Gajda, M. Kuball, Buffer transport mechanisms in intentionally carbon doped GaN heterojunction field effect transistors, *Appl. Phys. Lett.* 104 (2014), 263505, <https://doi.org/10.1063/1.4885695>.
- [34] G. Meneghesso, M. Meneghini, R. Silvestri, P. Vanmeerbeek, P. Moens, E. Zanoni, High voltage trapping effects in GaN-based metal–insulator–semiconductor transistors, *Jpn. J. Appl. Phys.* 55 (2016), 01AD04, <https://doi.org/10.7567/JJAP.55.01AD04>.
- [35] A. Armstrong, A.R. Arehart, D. Green, U.K. Mishra, J.S. Speck, S.A. Ringel, Impact of deep levels on the electrical conductivity and luminescence of gallium nitride codoped with carbon and silicon, *J. Appl. Phys.* 98 (2005), 053704, <https://doi.org/10.1063/1.2005379>.
- [36] U. Honda, Y. Yamada, Y. Tokuda, K. Shiojima, Deep levels in n-GaN doped with carbon studied by deep level and minority carrier transient spectroscopies, *Jpn. J. Appl. Phys.* 51 (2012), 04DF04, <https://doi.org/10.1143/JJAP.51.04DF04>.
- [37] J.L. Lyons, A. Janotti, C.G. Van de Walle, Carbon impurities and the yellow luminescence in GaN, *Appl. Phys. Lett.* 97 (2010), 152108, <https://doi.org/10.1063/1.3492841>.
- [38] V. Joshi, A. Soni, S.P. Tiwari, M. Shrivastava, A comprehensive computational modeling approach for AlGaIn/GaN HEMTs, *IEEE Trans. Nanotechnol.* 15 (2016) 947–955, <https://doi.org/10.1109/TNANO.2016.2615645>.
- [39] *Sentaurus Device User Guide Version I-2013.12*, Synopsys Inc., Mountain View, CA, USA, 2013.
- [40] S. Strauss, A. Erlebach, T. Cilento, D. Marcon, S. Stoffels, B. Bakeroot, TCAD methodology for simulation of GaN-HEMT power devices, in: 2014 IEEE 26th International Symposium on Power Semiconductor Devices IC's (ISPSD), 2014, pp. 257–260, <https://doi.org/10.1109/ISPSD.2014.6856025>.
- [41] F.A. Marino, D. Bisi, M. Meneghini, G. Verzellesi, E. Zanoni, M.V. Hove, S. You, S. Decoutere, D. Marcon, S. Stoffels, N. Ronchi, G. Meneghesso, Breakdown investigation in GaN-based MIS-HEMT devices, in: 2014 44th European Solid State Device Research Conference (ESSDERC), 2014, pp. 377–380, <https://doi.org/10.1109/ESSDERC.2014.6948839>.
- [42] K. Kunihiro, K. Kasahara, Y. Takahashi, Y. Ohno, Experimental evaluation of impact ionization coefficients in GaN, *IEEE Electron Device Lett.* 20 (1999) 608–610, <https://doi.org/10.1109/55.806100>.